Journal of Industrial and Engineering Chemistry 145 (2025) 430–440

Contents lists available at ScienceDirect

Journal of Industrial and Engineering Chemistry

journal homepage: www.elsevier.com/locate/jiec

Full Length Article

Optically active carbon dot/cellulose nanocrystal hydrogel printing inks with two-step authentication

Egor O. Ryabchenko, Arseniy P. Suslov, Chantal T. Tracey, Elena F. Krivoshapkina *

Energy Lab, ITMO University, 9 Lomonosova Street, St. Petersburg 191002, Russian Federation

ARTICLE INFO

Keywords:
Cellulose nanocrystals
Carbon dots
3D printing
Hydrogels
Anticounterfeiting
Two-factor authentication

ABSTRACT

The counterfeit market in field of consumer goods is still a great obstacle to financial well-being for manufacturers and consumers. Security labels with hidden images have proven to be an effective anticounterfeiting measure. Three-dimensional (3D) printing is an effective approach to fabricating labels with complex geometries using environmentally friendly and cost-effective customized inks. In this work, optically active hydrogels were made by incorporating fluorescent carbon dots (CDs) into a cellulose nanocrystal (CNC) matrix. The CD:CNC ratios were optimized to obtain inks with high viscosity and fidelity that exhibited shear-thinning behavior. The resulting inks showed good printability and the extrusion parameters were optimized to achieve high printing accuracy. When excited at different wavelengths, the printed patterns fluoresced different colors. CNC also showed shear-induced alignment upon extrusion, which is visible under polarized light, allowing hidden images to be incorporated into the printed structures for two-factor authentication.

Introduction

According to reports, from 1997 to 2022, the global counterfeiting market was estimated to be worth between US$35 and US$560 billion annually [1–6]. Counterfeiting, fraudulent imitation with the intent to deceive, evokes mistrust of products made by trusted brands, resulting not only in loss of revenue due to fewer consumer purchases and equity investments, but also in loss of reputation due to reduced consumer confidence, related diseases, and legal liabilities [7–9]. Food counterfeiting damages positive brand images, infringes on the rights of intellectual property holders, and benefits from the innovation, research and development, and marketing of recognized brands; as such, well-known brands spend hundreds of millions of dollars and thousands of hours each year to combat this problem (Fatima, 2023; [10]). Anti-counterfeiting, the act of preventing the production or reducing the existence of counterfeit goods, encompasses several protection measures designed to protect intellectual property by verifying the authenticity of an item [11–13]. Anti-counterfeiting measures include the registration of trademarks and patents, market monitoring, chain security, and cooperation with law enforcement agencies; however, these measures provide very limited protection due to territorial restrictions, patent expiration, poor item tracking, and poor authentication measures [14,7,8]. Recent studies have shown that security labels a more suited to minimizing counterfeiting [15–18].

In addition to preventing theft and ensuring product quality and safety by clearly indicating tampering, security labels are also used to guarantee product authenticity [13,19–21]. Security labels, which are explicit or implicit markings designed with special security features, are designed to reassure consumers that they are receiving genuine food products. These include void labels, QR codes, barcodes, tamper-evident seals, scratch-off labels, and serial number stickers; however, these types of labels can be easily replicated, so more intricate, difficult-to-replicate labels are needed to ensure product authenticity [14,22–24]. Hologram stickers and holographic overlays, security labels that display hidden images or patterns that appear three-dimensional or change color when viewed from certain angles, have proven to be particularly effective anti-counterfeiting measures [25–27]. Unfortunately, environmentally unsafe and relatively expensive materials such as lithium niobate, lead-containing perovskites, and silver halogenates are used to make these types of security labels [28–30]which excludes its usage for many consumer goods. As such, an environmentally friendly approach to the production of these hidden chromogenic images is needed. Studies have shown that three-dimensional (3D) printing can be used to create inexpensive security labels using environmentally friendly materials

* Corresponding author.
E-mail addresses: ryabchenko@scamt-itmo.ru (E.O. Ryabchenko), suslov@scamt-itmo.ru (A.P. Suslov), tracey@scamt-itmo.ru (C.T. Tracey), kef@scamt-itmo.ru (E.F. Krivoshapkina).

https://doi.org/10.1016/j.jiec.2024.10.038
Received 23 July 2024; Received in revised form 3 October 2024; Accepted 17 October 2024
Available online 22 October 2024

[31–33].

Three-dimensional printing is a type of additive manufacturing process in which a structure is created through the layer-by-layer deposition of a material [34–36]. Subdivided into stereolithography, which creates structures by curing layers of photosensitive materials via exposure to ultraviolet (UV) irradiation [37,38]; electrical deposition, which uses electrically charged particles to create 3D objects [39,40]; J. [41]; and extrusion methods, which are based on the deposition of a filament or gel [42–45], 3D printing has emerged as a convenient and simple method that provides high resolution, speed, and accuracy for fabricating structures, including optically active security labels for anti-counterfeiting. Extrusion-based 3D printing in particular has garnered attention due to one more important advantage: the ability to develop specialized, customized inks [44,46,47]. Typically, the developed inks consist of a base and incorporated functional materials dispersed throughout this matrix [42,48,45]. The base material is responsible for the printability and rheological properties of the ink, which enable the formation of the desired structure; therefore, the most suitable substrate materials are bio- and synthetic polymers [49]. On the other hand, dispersible functional materials are usually active inorganic nanoparticles that provide the printed structures with specific exploitable properties, such as electrical conductivity, magnetic responsivity, and optical properties [50–52]. Moreover, extrusion printing by gels makes possible to print patterns at different types of packaging due to high gels adhesion [53] which possess a great advantage for food packaging consist on a wide field of materials including conventional and innovative.

Cellulose nanocrystals (CNCs) are cost-efficient, biodegradable, environmentally friendly nanobiopolymers produced via the acid hydrolysis of microcrystalline cellulose [54,55]. CNCs are a self-assembling array of nanomaterial with interesting rheological and optical properties that form a left-handed chiral nematic crystal means rods twisted perpendicular to director axis [56,57]. CNC exhibits non-Newtonian shear thinning, with its viscosity decreasing with increasing mechanical stress, making it a suitable base material for gel inks [58]. Mechanical stress also alters the liquid crystalline structure of CNC suspensions, leading to deformation and affecting nanoparticle orientation; as such, extrusion may result in the formation of specific patterns. Similarly, carbon dots (CDs) have unique optical properties, which make them suitable functional dispersants in customized inks designed for the development of optically active security labels [59,60]. Inexpensive and easy-to-synthesize carbon-based nanoparticles less than 10 nm in size, biocompatible CDs are highly sought after for their fluorescent and photoluminescent properties, which can be controlled by the synthetic method and precursors used, making them popular functional components of inks designed for imaging applications [61,60].

We hypothesize that, by combining the shear-induced polarization of CNC with the intrinsic fluorescence of CDs, it is possible to create intricate security labels with two degrees of protection. As with all fluorescent objects, the label would fluoresce when irradiated with monochromatic (*e.g.*, UV) light. However, in the event that the fluorescence of the pattern is imitable, the shear-induced optical properties of the base CNC material would enable a second-order hidden image that is only visible under polarization lenses to be incorporated into the printed structure. By using two different-colored fluorescent inks with this effect to make the final structure, a single label may have at least three decipherable images. In this work, we present novel, cheap, environmentally friendly CD/CNC hydrogel inks for security printing with two-step authentication using two optical effects simultaneously.

Materials and methods

Materials

Citric acid (CA, 99.5 %), urea (99.0 %), dimethylformamide (DMF, anhydrous, 99.8 %), quinine sulfate (90.0 %), and Rhodamine 6G (99.0 %) were obtained from Sigma-Aldrich. Ethanol (96.0 %), hydrochloric acid (HCl, 1 M), and sulfuric acid (H_2SO_4, 0.5 M) were supplied by Petrospirt (Russian Federation). Cellulose nanocrystal (CNC) suspension (9.8 wt%) was purchased from CelluForce (Canada). All reagents were analytical grade and used without further purification.

An Aquilon D-301 purification system was used to deionize and purify water to a conductivity of 18.2 MΩ·cm.

Carbon dot synthesis

CD synthesis was conducted according to the method described by [62]. In the current work, two types of CDs were synthesized: blue-emissive CDs (BCD) and red-emissive CDs (RCD). For BCD, CA (2 g) and urea (4 g) were dissolved in water (20 g). After their complete dissolution, the mixture was introduced to a 30 mL PTFE-lined autoclave that was subsequently sealed and heated in an oven at 180 °C for 4 h. The resulting dark-green liquid was washed with ethanol then water to remove organic contaminants and unreacted precursors via centrifugation at 12000 rpm for 20 min. The sediment was then collected and freeze-dried at –20 °C. The resulting powder was stored until further use. To obtain RCD, the procedure was repeated except that CA and urea were dissolved in DMF instead of water. A schematic diagram of the synthetic procedures is presented below (Scheme 1):

Carbon dot characterization

CD particle size was determined using dynamic light scattering (DLS), which was performed on a Photocor Compact Analyzer (Photocor, Russian Federation). Transmission electron microscopy (TEM) images of BCD and RCD were obtained on a HT-7700 transmission electron microscope (Hitachi, Japan). CD optical properties were evaluated using ultraviolet–visible (UV–Vis) spectroscopy, which was performed using a Cary 60 double-beam spectrophotometer (Agilent Technology Inc., USA), and spectrofluorimetry, which was conducted on a Cary Eclipse spectrofluorometer (Agilent Technologies Inc., USA) equipped with a xenon lamp as a light source.

CD photoluminescence quantum yield (PLQY) was determined using quinine sulfate dissolved in 0.5 M H_2SO_4 (λ_{em} = 451 nm, QY = 54.6 %) and Rhodamine 6G dissolved in water (λ_{em} = 567 nm, QY = 92.0 %) as standards in accordance with their PL wavelengths [63,64]. For BCD, several quinine sulfate solutions and BCD suspensions with different concentrations were prepared. Their measured absorbances did not exceed 0.1. QY was determined using the following equation [65]:

$$QY_x = QY_{st} \bullet \left(\frac{m_x}{m_{st}}\right)\left[\frac{(n_x)^2}{(n_{st})^2}\right] \quad (1)$$

where m_x and m_{st} are the slopes of the sample and standard, respectively; and n_x and n_{st} are the refractive indices of the solvents used for the samples and standard, respectively. The procedure was repeated for

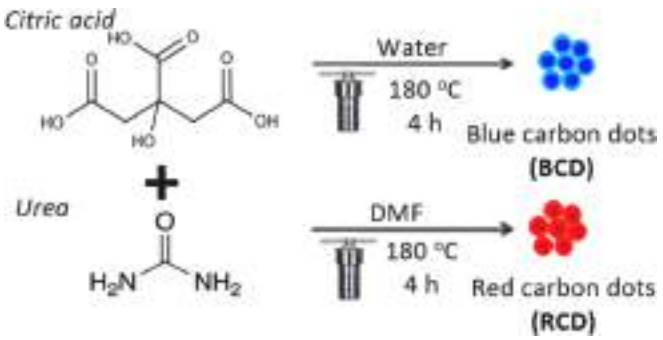

Scheme 1. Schematic diagram of CD synthesis.

RCD using Rhodamine 6G as the standard.

Ink preparation and optimization

Ink preparation

CD and CNC inks were mixed in different ratios to determine the sol–gel transition regions and optimal compositions. To obtain the ink, freeze-dried BCD powder was dispersed in water at a concentration of 100 mg/mL. The resulting dispersion was then mixed with CNC (9.8 wt %) at various CNC:CD ratios. The mixtures were vigorously shaken using a vortex mixer until the nanoparticles were uniformly distributed. The procedure was repeated to obtain RCD/CNC inks. The zeta (ζ) potentials of the base and added functional materials were measured using laser Doppler electrophoresis (LDE) on the Photocor Compact Analyzer. Scanning electron microscopy (SEM) images of BCD/CNC and RCD/CNC gels were captured using a Vega 3 scanning electron microscope (Tescan, Czech Republic). Fourier transform infrared (FTIR) at a range 400–4000 cm^{-1}, which was performed on a Nicolet iS5 spectrometer (Thermo Scientific, USA), was used to determine changes in chemical structure between dried CD samples and obtained inks. Considering rheology and pH changes during protonation, pH was measured using a P21 glass electrode for colloids (Sentek LTD., United Kingdom).

A DHR-1 rheometer (TA Instruments, USA) with a conical (2°) plate geometry was used for all rheological experiments. The tensile elastic modulus of each ink was measured using an LS 1 universal testing machine (Lloyd Instruments, United Kingdom). All rheological experiments were performed at 20 °C.

Shear behavior

The shear behaviors of the optimized inks were investigated to prove that the mechanical

force applied by the printhead decreases ink viscosity and that extrusion can occur without leakages or underfilling. The obtained inks were incubated under ambient conditions for 1 h before analysis. The shear behaviors of BCD/CNC and RCD/CNC were studied by increasing the shear rate from 0.01 to 100.0 s^{-1} and then analyzed by their viscosity to find the optimal ink compositions for printing.

Ink fidelity

To investigate the recovery properties of the inks, a periodic step test with conditioning of gel under 0.01 s^{-1} and 30.0 s^{-1} was performed. The obtained inks were incubated under ambient conditions for 1 h before analysis. The test, which consisted of three cycles, entailed extruding the ink at 0.01 s^{-1} before sharply increasing the shear rate to 30.0 s^{-1} with further conditioning. The first two cycles with shear rate changes are used to compare the difference between viscosities in low-shear stages. The third cycle was used as a control in order to exclude any anomalies in measurements. The second and third viscosity measurements should be equal.

Ink physical stability

To determine and compare ink physical stability, BCD/CNC, RCD/CNC and neat CNC solution was investigated for their elastic (G′) and viscous (G″) moduli determination. The viscoelastic responses of the hydrogel samples were recorded in range from 1 to 5000 Pa.

Ink optical stability

Weathering imitation (light and temperature exposure, humidity) for CDs and patterns printed from inks were performed by exposing gels inside a UV-chamber Momax UV-Box (Momax, China) modified with heaters and humidifier. CDs were exposed to UV light for 24 h, to sunlight for 30 days, and the samples were heated up to 80 °C for 24 h to study their photostabilities through comparison of their emission spectra at their optimal emission wavelengths (λ_{em}). To avoid evaporation-induced quenching due to volume changes, CD samples were heated under reflux conditions.

For BCD- and RCD-based optically active security labels, the same experiments (light exposure, heating) were conducted; however, humidity stability testing was also performed. The humidity in the chamber was controllably set as 20, 40, 60 and 80 % and samples were exposed for 7 days. Changes in pattern geometry and integral fluorescence intensity for printed inks were investigated using a DMi8A microscope (Leica, Germany).

Mechanical properties of films cast and printed from inks

The mechanical properties of the inks were studied by preparing films for mechanical studies. For dynamic mechanical analysis, the films were divided into cast and aligned samples. Cast samples were prepared by applying inks on a PDMS substrate then curing at 20 °C for 12 h. The aligned samples were printed with inks in a specific direction before being cured at 20 °C for 12 h. The mechanical properties of the films were studied by dynamic mechanical analysis in tensile (stretching) tests of the films formed by inks dried under ambient conditions. The tensile elastic moduli (E_T) of films obtained by extruding ink in one direction and cast films were measured. The adhesion and impact resistivity of the cast and printed films were also analyzed (ISO 4624:2023 Paints and Varnishes Pull-off Test for Adhesion, 2023), (ISO 6272–1:2011 Paints and Varnishes; Rapid-Deformation (Impact Resistance) Tests, 2011). For impact resistance tests, the inks were deposited onto a metal plate. For adhesion resistance test, inks were deposited on different substrates to show its universality in being printed on various packages: metal plate, polyethylene terephthalate (PET), polyvinylchloride (PVC), low density polyethylene (LDPE), polypropylene (PP), polystyrene (PS), silicate-boron food-grade glass (FG).

Printing

All models for 3D printing were developed using Autodesk Fusion 360 software. Cellink Heartware was used for GCode editing and extruder movement analysis. Additive manufacturing was performed with a Cellink Bio X gel extrusion bioprinter (BICO, Sweden). Printing parameters were optimized for accuracy and precision. All optimization experiments consisted of step-by-step analysis of parameter influence on corresponding coefficient (**Equation (2)** between model and structure.

$$C_{\%} = \left(1 - \left(\frac{|X_M - X_S|}{X_M} + \frac{|Y_M - Y_s|}{Y_M} + \frac{|Z_M - Z_S|}{Z_M}\right)\right) \times 100\% \quad (2)$$

where X_M, Y_M, and Z_M are the geometrical parameters of the model and X_S, Y_S, and Z_S are the geometrical parameters of the printed structure.

Optimal printing parameters were determined by varying a single parameter while the others remained constant to avoid any negative effects in extrusion caused by inconvenient process parameters.

Fluorescent, optical, and polarization microscopy images of the printed patterns were obtained on a DMi8A microscope (Leica, Germany).

Results and discussion

Carbon dot characterization

After synthesis and purification, DLS showed that BCD and RCD have uniform size distributions of 2 – 4 nm and 5 – 8 nm, respectively. TEM images (Fig. 1**a, 1b**) confirmed CD particle size. The optical properties of BCD and RCD were then studied. UV–Vis spectroscopy was performed to determine the absorption peaks for both types of CDs. As shown in Fig. 1**c**, λ_{max} for BCD and RCD were 344 nm and 549 nm, respectively. Then, spectrofluorimetry was performed to further investigate the optimal wavelengths for excitation and emission. The optimal

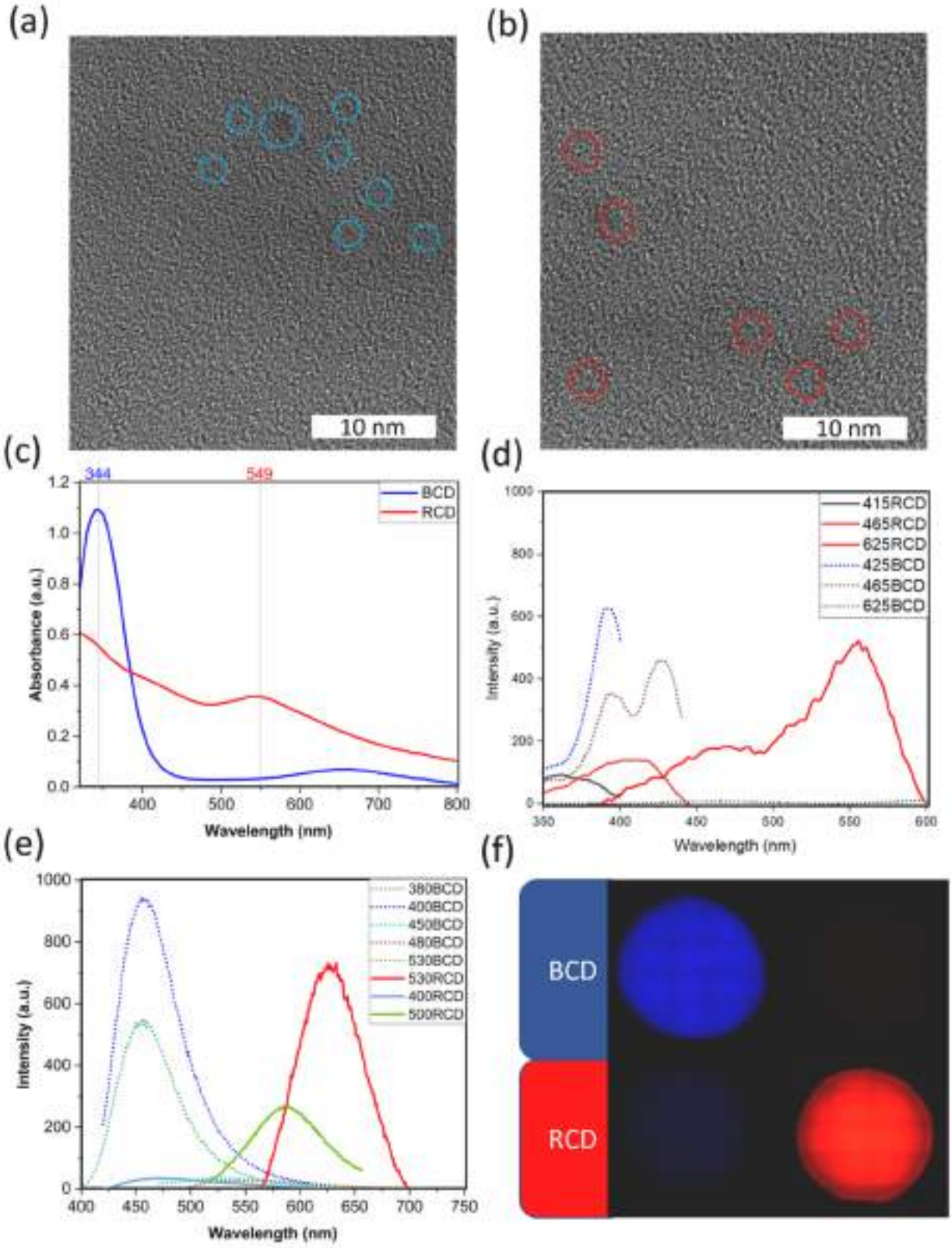

Fig. 1. TEM image of (a) BCDs and (b) RCDs; circles in the TEM images highlight CDs within the micrographs. (c) BCD and RCD UV–Vis absorption spectra. (d) BCD and RCD excitation spectra. (e) BCD and RCD emission spectra. (f) Microscope images of droplets from BCD and RCD under different monochromatic light: 380 nm (left image) and 535 nm (right image).

wavelengths for excitation (λ_{ex}, Fig. 1**d**) and emission (λ_{em}, Fig. 1**e**) were determined to be 380 nm and 465 nm, respectively, for BCD and 530 nm and 625 nm, respectively, for RCD. The excitation and emission bands are markedly different, and the BCD and RCD do not overlap each other in the blue and red wavelength bands. In addition, Fig. 1**f** shows the images of CDs under fluorescence microscope excitation. As can be seen from the figure, the two colors are distinct under two different filter cubes. The difference between the excitation and emission wavelengths for BCD and RCD allows the creation of multi-colored patterns that show two different images upon irradiation, which can be used as a first-order anticounterfeiting measure.

The PLQYs of BCD and RCD were determined to be 32.6 % and 43.8 %, respectively, which is higher than that of CDs reported in the literature [66–68]. The difference between BCD and RCD PLQYs may be attributed to the degree of nitrogen doping of the carbon structures [62]. The solvothermal synthesis of RCD in DMF led to the formation of more C = O and C = N bonds, which are responsible for the longer emission wavelength. Furthermore, due to the differences in synthesis, RCD has fewer non-radiative traps than BCD, which may also explain its higher PLQY (M. [69]. BCD and RCD having high PLQYs allow them to fluoresce brightly when illuminated with monochromatic light. As shown in **Figure S1**, BCDs and RCDs PL intensity remained relatively stable after light irradiation and temperature exposure, indicating that any printed pattern will remain visible for at least 30 days, making them suitable for commercialization [70].

FTIR shows significant differences between BCD and RCD and their precursors (**Figure S2**). The described zone between 1200 and 1800 cm^{-1} exactly corresponds with the original study, the peak 1542 cm^{-1}, indicating the presence of aromatic carbon. The broad peaks between 2000 and 3750 cm^{-1} (also overlapping with amine peaks) indicates the presence of a large number of hydroxyl groups on both the BCD and RCD surface. The peak at 1340 cm^{-1}, which was attributed to amine groups, overlaps with the aromatic carbon peak for RCD due to higher carbonization degree [71–73]. The weak peak at 1032 cm^{-1} was attributed to C-N bonding typical for amines. The shift between the original precursors' peaks (especially observable for citric acid) also suggest the formation of a carbonized structure due to an increase in compound atomic mass, which is observed for both BCD and RCD [70,60,62].

CD/CNC ink preparation, characterization, and optimization

CNC and CD were mixed together obtain hydrogel inks (Fig. 2**a,b**). As mentioned above, both BCD and RCD had negative ζ potentials. However, the ζ potential of CNC was also negative (−26.1 ± 0.6 mV); thus, gel formation should not have occurred due to electrostatic repulsion between CNC and CD nanoparticles [74–76]. The observed gelation may be attributed to the protonation of BCD and RCD upon introduction to the acidic CNC medium ($pH_{CNC} = 5$). For CDs, especially those that are amino-rich, protonation in acidic media can significantly increase the ζ potential, sometimes resulting in a change in charge [77]. To test this hypothesis, the pHs and corresponding ζ potentials of BCD and RCD were measured. The original BCD suspension had a pH of 8 and a ζ potential of −9.25 ± 0.17 mV while the initial RCD suspension had a pH of 9.3 and a ζ potential of −10.8 ± 0.4 mV. Hydrochloric acid (1 M) was used to lower the pHs of both suspensions to pH 5, which is the pH of the CNC suspension. After pH correction and protonation, the ζ potentials of BCD and RCD increased to +3.14 ± 0.87 mV and +5.26 ± 0.55 mV, respectively. This change in charge resulted in electrostatic attraction between CNC and the now-protonated CDs, leading to gelation. It should be noted that both BCD and RCD showed different

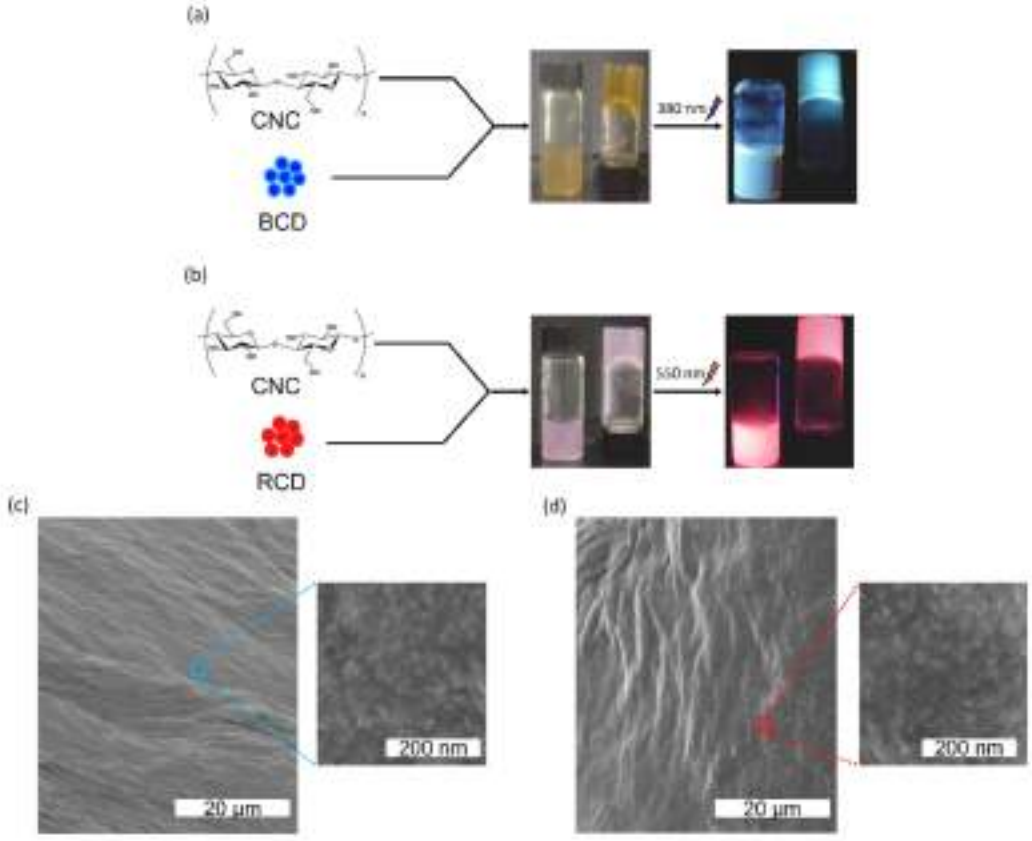

Fig. 2. (a) Schematic of BCD/CNC colloidal gel ink formation and its photoluminescence at 380 nm. (b) Schematic of RCD/CNC colloidal gel ink formation and its photoluminescence at 550 nm; SEM images of (c) BCD/CNC and (d) RCD/CNC hydrogels.

electrokinetic potentials in aqueous medium and in cellulose nanocrystal solution medium. The gelation process in the CD/CNC system occurs between pH 5.68 and pH 7.12, which was measured for the colloidal system.

The resulting hydrogels remained optically active, glowing blue and red upon irradiation (Fig. 2**a,b**). BCD/CNC and RCD/CNC gels were lyophilized to obtain powders that were then analyzed using SEM (Fig. 2**c,d**), FTIR (**Figure S2**).

According the SEM images, hydrogel films BCD/CNC and RCD/CNC has continuous and dense surface structure observed for the material ~~is due~~ reasoning by influence of various intramolecular forces arising from the interaction of cellulose chains and CDs.

The FTIR spectra of BCD/CNC and RCD/CNC are similar (**Figure S2**). For BCD and RCD gel formation with cellulose causes the peak at 1026 cm^{-1} (ascribed to C-O in glucopyranose units) to shift to 1015 cm^{-1} for BCD/CNC and to 1022 cm^{-1} for RCD/CNC [78–80]. Moreover, the peaks responsible for –OH for CNC and CDs weakened; however, the peaks that may be attributed to the presence of amine salts (broad peak in region 3000–3500 cm^{-1}, asymmetric and symmetric bends at 1625 cm^{-1} and 1544 cm^{-1}) emerge [81–83]. This indicates that gel formation occurs through interaction between the hydroxyl groups of CNC and protonated amino groups [81,84,85].

CD and CNC were mixed in different ratios to study their sol–gel transitions. As can be seen from Fig. 3**a,b**, less RCD than BCD was needed to form suitable hydrogels. The differences in BCD:CNC and RCD:CNC gelation ratios can be explained by differences in the chemical natures of BCD and RCD, namely carbonization degree as well as the type and number of functional groups on the BCD and RCD surfaces [86,60]. For CDs, the degree of carbonization directly influences the number of surface functional groups as well as their distribution, which in turn affects protonation. In acidic media, RCD had a higher ζ potential than BCD, suggesting stronger protonation and, therefore, greater electrostatic attraction to CNC, resulting in better gel formation. This may be attributed to the greater number of amino groups on the RCD surface. RCDs were synthesized in DMF, which resulted in mainly amino groups on their surface [86,87].

As shown in Fig. 3**a,b**, the regions corresponding to gel formation are broad for both BCD/CNC and RCD/CNC; therefore, it is necessary to determine the optimum ratio for printing. This was done by investigating how the viscosities of inks with m(CD)/m(CNC) ratios between 1 and 10 varied with shear rates between 0.01 s^{-1} and 30.0 s^{-1} [76]. As shown in Fig. 3**c**, the optimum CD:CNC ratio for BCD was 0.3 while that for RCD was 0.6. The viscosity of the CD/CNC inks under shear stress was also used to confirm gel formation by comparing their viscosities with that of the original CNC suspension. The optimized BCD/CNC and RCD/CNC inks had viscosities of 19855.6 and 2477.5 Pa·s at 0.01 s^{-1}, respectively, confirming gelation.

As shown in Fig. 4**a**, both BCD/CNC (blue) and RCD/CNC (red) exhibit non-Newtonian shear thinning and their viscosities (η) decrease with increasing shear rate (γ), with the viscosity of BCD/CNC (blue) decreasing smoothly from 19720 ± 854 to 2.83 ± 0.12 Pa·s while that of RCD/CNC (red) decreases from 2522 ± 122 to 0.41 ± 0.18 Pa·s. Such flow behavior indicates non-linear viscoelastic properties and, therefore, stable continuous flow from the printhead. Moreover, the smooth shear flow curve suggests sample homogeneity, indicating that the resulting structure will likely be able to support itself during and after printing, which means high accuracy of manufactured structures [88].

Another important ink property is fidelity, which is the rate at which the viscosity recovers after shear reduction, *i.e.*, the self-healing properties of the ink. In 3D printing, good viscosity recovery means satisfactory gel shape formation after extrusion onto a substrate; thus, the transition time from solid to liquid then back to solid should be as short as possible. Short transition times enable printing with high speed and accuracy [76,89]; however, if the transition time is too long, printing is arduous, which is unideal for process scaling. BCD/CNC had a recovery rate of 80.3 ± 0.5 %, with the viscosities in the first and second cycles being 19778 ± 996 and 15804 ± 655 Pa·s, respectively (Fig. 4**b**), while RCD/CNC had a recovery rate of 63.2 ± 0.3 %, with the viscosity decreasing from 2478 ± 125 Pa·s in the first to 1566 ± 76 Pa·s in the second cycle (Fig. 4**c**). The gels exhibit reversible shear thinning viscoelastic behavior, which confirms their printability and will enable their accurate deposition onto a substrate.

All inks showed typical gel-like properties in analysis of elastic (G′) and viscous (G″) moduli due to the dominance of G′ over G″ (**Figure S3**). Compared to pure CNC solution, the obtained hydrogels were significantly more stable according to the width of the linear viscoelasticity range, which directly show the strength of polymer network [90,91,79]. CNC, BCD/CNC, and RCD/CNC gels lose their gel-like behavior at 116, 1542, and 503 Pa, respectively. These differences indicate increasing gel network strength, resulting in remarkable physical stability of the hydrogels.

Stability of optical activity

After prolonged exposure to UV light and sunlight, the printed samples did not show any significant changes. The integral loss of emission intensity for BCD/CNC was 1.3 % under UV light and 1.5 % under sunlight. For RCD/CNC, the integral loss was 1.4 % and 2.1 %, respectively. To investigate heat stability, line-like printed patterns were prepared (**Figure S4**). As shown, there are no significant changes in polarization; however, fluorescence quenching is observed. After continuous heating at 80 °C for 24 h, BCD/CNC and RCD/CNC has lost 12.2 % and 15.6 % of their emission intensity, respectively. This quenching was attributed to a decrease in the distance between CDs due to the active evaporation of water molecules from the surface [92,93]. Moreover, the pattern for RCD has a few geometrical differences by its square size (0.51 %) after heating. Continuous exposure to humidity does not cause any noticeable changes in fluorescence intensity, geometrical size, or polarization patterns for the printed labels and it is independent from the period or the humidity percentile.

Summarizing, the printed labels have relatively low resistance to the high temperatures. However, for temperatures in excess of 80 °C for many consumer goods often means that the product currently in use. Nevertheless, it limits the scope of application of these types of labels, especially those that involve high temperatures (*e.g.*, metal car parts and heating equipment).

3D printing optimization

To determine optimum printing conditions, a model structure was printed under default parameters where pressure = 20 kPa, ink and substrate temperatures = 20 °C, and printing speed = 30 mm·s^{-1}. In this work, precision is given in percentages. A parallelepiped 20 × *B* × *C* mm structure was modeled, where *B* is equal to the diameter of the inner extrusion unit and is also equal to the layer height, *C*. After printing under different parameters, the resulting prints were compared to the default print. The structure should not have any leakages, non-extruded parts and the total area and volume has to correspond with original model geometry. Error estimates for pressure, temperature difference and speed are provided during the optimization process. For each evaluation, the other parameters are fixed as constants. In Table 1, all parameters for the best performance are estimated with an error that describes the geometric deviations from the CAD-designed models. Regarding the extruder for speed and temperature testing, we evaluate the unit obtained from the pressure evaluation with the lowest error rate among the other optimal error rates. This was a needle with a diameter of 0.41 mm for BCD/CNC and 0.25 mm for RCD/CNC. The comparatively smaller optimal inner diameter of the RCD/CNC extruder can be attributed to rheological differences between RCD/CNC and BCD/CNC. As shown above, BCD/CNC has a higher viscosity, better shear thinning behavior, and higher fidelity than RCD/CNC. As such, much lower pressure can be applied to extrude RCD/CNC inks. Moreover, the lower

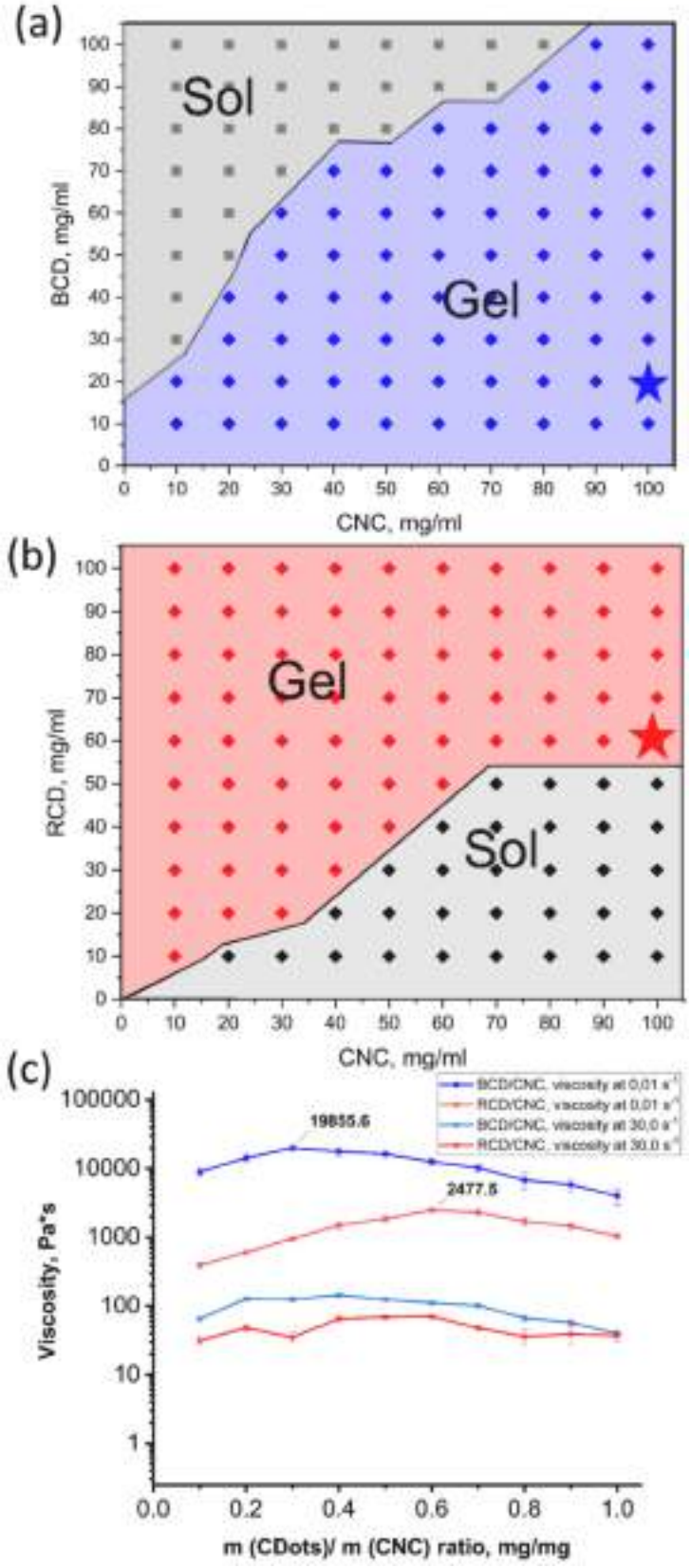

Fig. 3. Sol-gel phase diagram for (a) BCD/CNC and (b) RCD/CNC inks with different CD:CNC ratio. (c) Viscosity under different shear rates for BCD/CNC and RCD/CNC with different CD:CNC ratios (optimum CD:CNC ratios are highlighted).

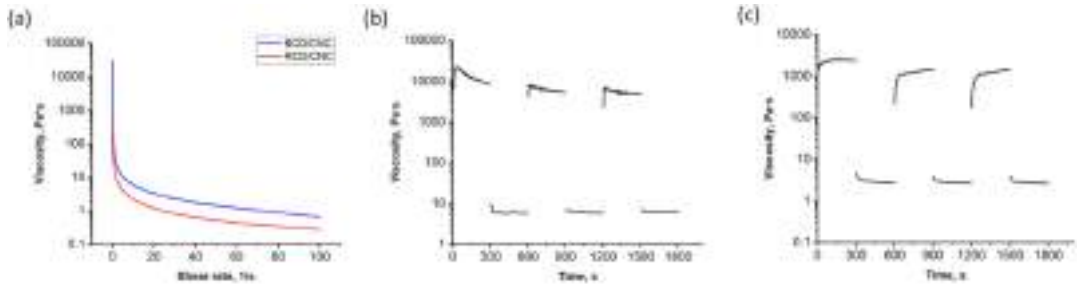

Fig. 4. (a) Variation of shear rate and viscosity measurements for optimized inks. Fidelity test and ramp viscosity measurements for (b) BCD/CNC and (c) RCD/CNC at 0.01 s^{-1} and 100.0 s^{-1}.

Table 1
Optimum parameters for 3D printing of BCD/CNC and RCD/CNC inks.

Ink	Extrusion pressure (Pa•s)				Temperature (°C)		Speed (mm·s^{-1})	Error rate (%)
	Inner diameter (mm)				Ink	Substrate		
	0.52	0.41	0.25	0.21				
BCD/CNC	12	16	24	36	20	10	25	0.5
RCD/CNC	8	12	20	20				0.20

the pressure, the greater the influence of the fidelity factor, which also provides better printability for RCD/CNC inks. With this variation, the optimal printing parameters were determined, with compliance rates of 0.46 % and 0.20 % for BCD/CNC and RCD/CNC, respectively.

Mechanical properties of printed structures

In CD/CNC films, a difference was observed between the results based on tensile direction and its correspondence for shear-induced alignment of CNC. When stretched, the cast films with randomly aligned CNCs are less elastic than the horizontally extruded films that were stretched in one direction. However, stretching the printed film in a direction that does not correspond to the print alignment leads to a lower elastic modulus. The results for CD/CNC are consistent with the tensile behavior of polymer fibers applied randomly and via 3D printing when stretched parallel to the extrusion direction [94]. With proper implementation of structure into commercial goods (*e.g.*, packaging with stretch films), it is possible to find an advantage here in front of films with random distribution of CNC due to being more resistant to tensile break.

Printed and casted films at metal plate substrate have coating adhesion 93 – 99 %, with minor advancements for printed films. Impact test has shown resistance to strike from heights 35 – 48 cm. Here, the advantage of printed films is more obvious, due to resistivity caused by specific alignment formation through extrusion. All obtained data by mechanical testing are shown in Table 2.

Table 2
Mechanical properties of tested BCD/CNC and RCD/CNC films.

Film and casting features	BCD/CNC, cast	BCD/CNC, extruded vertically	RCD/CNC, cast	RCD/CNC, extruded vertically
E_T, vertical stretching (MPa)	528 ± 72	665 ± 25	628 ± 53	721 ± 22
E_T, horizontal stretching (MPa)	531 ± 59	485 ± 61	633 ± 27	588 ± 17
Impact test results (cm)	36 ± 1	42 ± 1	44 ± 2	46 ± 2
Coating adhesion, metal plate (%)	95	98	96	97
Coating adhesion, PET (%)	99	99	99	99
Coating adhesion, PVC (%)	99	95	98	93
Coating adhesion, LDPE (%)	95	97	97	93
Coating adhesion, PP (%)	98	95	98	96
Coating adhesion, PS (%)	97	99	97	94
Coating adhesion, FG (%)	99	99	99	99
Average adhesion mark (according to ISO 2409)	0	0	0	0

Two-factor security labels

Autodesk Fusion software was used to create digital models that were then finalized in CellInk Heartware, which was used to incorporate second-order hidden structures. Fig. 5 shows all prepared patterns as imaged under a microscope equipped with fluorescent filter cubes and a polarization lens. Fig. 5**a,b** show a barcode printed using both BCD/CNC and RCD/CNC. When excited at λ_{ex} = 360 nm, only the part of barcode printed using the BCD/CNC ink fluoresced, giving off strong blue emission (Fig. 5**a**); however, the opposite is observed when the printed structure was excited at λ_{ex} = 530 nm, and only the parts of the barcode printed using the RCD/CNC hydrogel fluoresced, giving off strong red emission (Fig. 5**b**). In polarization mode (POM), at 90 degrees, the linear pattern consistent with extruder movements is visible. A hidden image was also encoded into the barcodes by changing the number of lines that made up each large line (LL). As shown in Fig. 5**a,b**, most of the visible LL consists of a single polarization line; however, some of the wider LLs consist of two, three, or five lines. Using this algorithm, the number "231131511111115" was hidden inside the barcodes (Fig. 5**a,b**).

For more intricate designs, it is possible to hide entire images within the polarization pattern. As shown in Fig. 5**c, a** square-like pattern consisting of three parts – BCD/CNC at the top, RCD/CNC at the bottom, and a 5 % CNC suspension droplet at the center of the model – was printed. Extrusion was top to bottom for the northwest and southeast quadrants and left to right for the northeast and southwest quadrants. The CNC drop was added after the printing process was completed. Microscopy showed that the lines in the pattern copied the extrusion directions. It is also possible to create patterns based only on GCode editing; thus, for this gel ink system, a new degree of protection based on

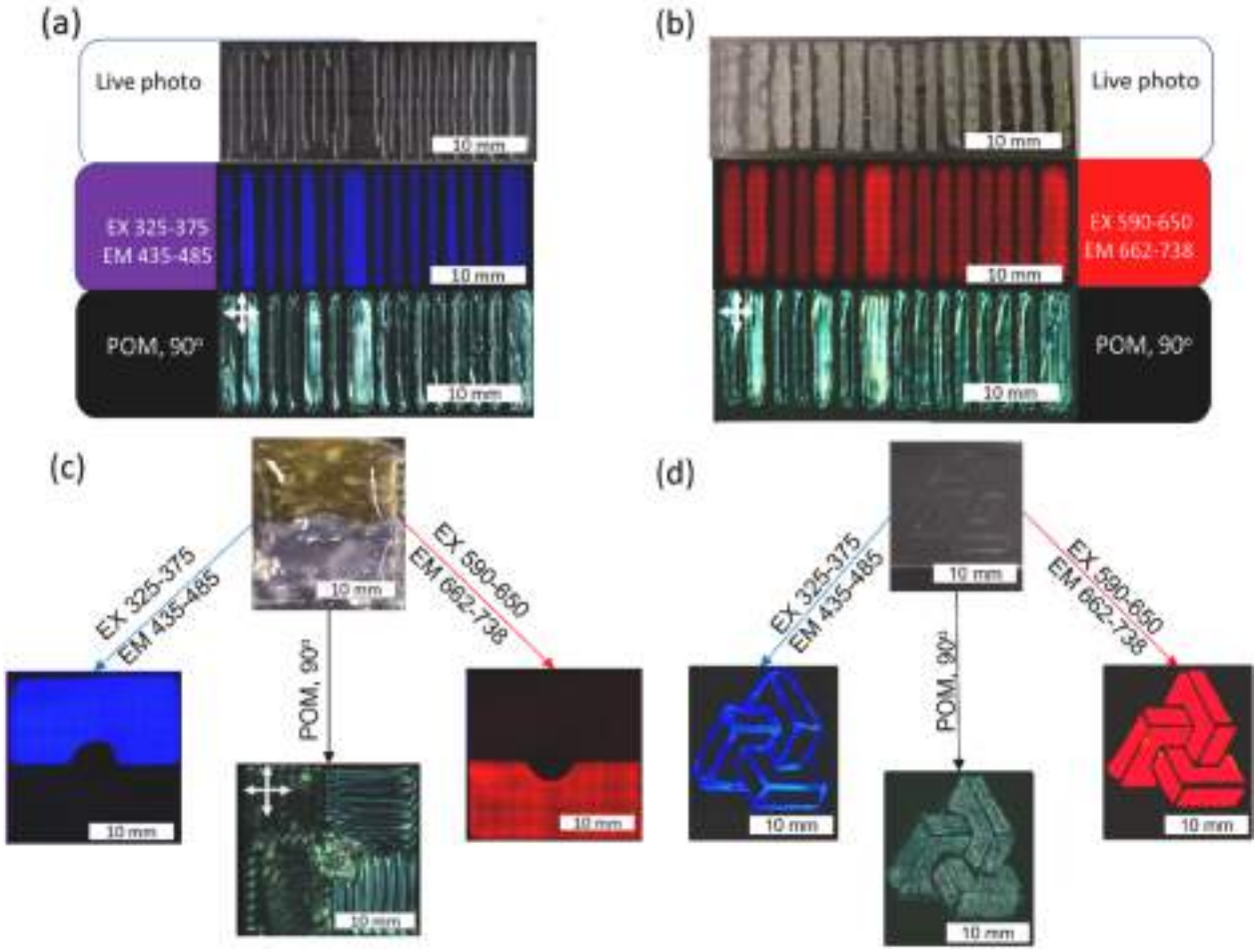

Fig. 5. (a) Barcode-like pattern printed with BCD/CNC and analyzed under fluorescence microscope through filter cube (second image), polarization lens (third image); (b) barcode-like pattern printed with RCD/CNC and analyzed under fluorescence microscope through filter cube (second image), polarization lens (third image); (c) complex square-like three-part pattern; (d) Escher-like pattern printed on glass.

the direction of extrusion during printing can be incorporated not. This approach was used to print Escher patterns (Fig. 5**d**) where BCD/CNCs served as the basic foundation before RCD/CNC droplets were deposited unto the surface. Under polarization, BCD/CNC nanoparticles are aligned while RCD/CNC nanoparticles have random orientation.

Conclusion

This work investigates the design and development of multi-protection inks based on carbon dots and cellulose nanocrystals for protection of consumer goods. Using both negatively charged components, we demonstrate an approach to form a physically cross-linked shear-thickening gel. As with previously investigated gels based on oppositely charged components, we have shown that gel formation also occurs within a certain range. Moreover, the inks adhesion for different substrates remarkable high which expand the field of application for labels based on them. Also in this work, we have demonstrated a multi-factor security 3D printing approach, one using fluorescent patterns and another based on polarization patterns visible only under a polarizing lens.

CRediT authorship contribution statement

Egor O. Ryabchenko: Writing – original draft, Methodology, Investigation, Formal analysis, Data curation, Conceptualization. **Arseniy P. Suslov:** Writing – original draft, Validation, Investigation, Formal analysis, Data curation. **Chantal T. Tracey:** Writing – review & editing, Visualization, Conceptualization. **Elena F. Krivoshapkina:** Writing – review & editing, Supervision, Project administration, Methodology, Funding acquisition, Conceptualization.

Declaration of competing interest

The authors declare that they have no known competing financial interests or personal relationships that could have appeared to influence the work reported in this paper.

Acknowledgements

This work was supported by the Russian Ministry of Science and Higher Education “Science and Universities” National Project state task No. FSER-2022-0002. E.F.K. also acknowledges the Priority 2030 Federal Academic Leadership Program for infrastructural support.

The authors would also like to thank Professor Eugenia Kumacheva (University of Toronto, Canada) for advice that led to the conceptualisation of this project.

Appendix A. Supplementary data

Supplementary data to this article can be found online at https://doi.org/10.1016/j.jiec.2024.10.038.

References

[1] V.N.M. Bharadwaj, M. Brock, B. Heing, R. Miro, U.S. Intellectual Property and Counterfeit Goods— Landscape Review of Existing/Emerging Research, 2020. https://www.uspto.gov/sites/default/files/documents/USPTO-Counterfeit.pdf.

[2] F. Rezazade, J. Summers, D.O. Lai Teik, A holistic approach to food fraud vulnerability assessment, Food Control 131 (2022) 108440, https://doi.org/10.1016/j.foodcont.2021.108440.

[3] K. Robson, M. Dean, S. Brooks, S. Haughey, C. Elliott, A 20-year analysis of reported food fraud in the global beef supply chain, Food Control 116 (2020) 107310, https://doi.org/10.1016/j.foodcont.2020.107310.

[4] C. Villano, M.T. Lisanti, A. Gambuti, R. Vecchio, L. Moio, L. Frusciante, R. Aversano, D. Carputo, Wine varietal authentication based on phenolics, volatiles and DNA markers: State of the art, perspectives and drawbacks, Food Control 80 (2017) 1–10, https://doi.org/10.1016/j.foodcont.2017.04.020.

[5] R. Xie, J. Zhang, S. Wen, R. Zhao, N. Wang, A. Chen, Rapid identification of escolar (Lepidocybium flavobrunneum) and oilfish (Ruvettus pretiosus) species based on recombinase polymerase amplification, Food Control 144 (2023) 109352, https://doi.org/10.1016/j.foodcont.2022.109352.

[6] H. ALI Nora, F. Fatima, Global trade in counterfeit products-facts & solutions, J. Contemporary Business Econ. Stud. (2023).

[7] Office of the United States Trade Representative. Review of Notorious Markets for Counterfeiting and Piracy, 2021.

[8] R. Pittiglio, Counterfeiting and firm survival. Do international trade activities matter? Int. Bus. Rev. 32 (5) (2023) 102145 https://doi.org/10.1016/j.ibusrev.2023.102145.

[9] M. Varela, P. Lopes, R. Mendes, Luxury brand consumption and counterfeiting: A case study of the Portuguese market, Innov. Mark. 17 (3) (2021) 45–55, https://doi.org/10.21511/im.17(3).2021.04.

[10] D. Bansal, Anti-Counterfeit Technologies: A Pharmaceutical Industry Perspective, Sci. Pharm. 81 (1) (2013) 1–13, https://doi.org/10.3797/scipharm.1202-03.

[11] A.F. Smith, S.E. Skrabalak, Metal nanomaterials for optical anti-counterfeit labels, J. Mater. Chem. C 5 (13) (2017) 3207–3215, https://doi.org/10.1039/C7TC00080D.

[12] S.J. Trenfield, H. Xian Tan, A. Awad, A. Buanz, S. Gaisford, A.W. Basit, A. Goyanes, Track-and-trace: Novel anti-counterfeit measures for 3D printed personalized drug products using smart material inks, Int. J. Pharm. 567 (2019) 118443, https://doi.org/10.1016/j.ijpharm.2019.06.034.

[13] Wu. Jiao, H. Ge, Review of Patented Technology of Magnetic Ink Anti-counterfeiting. In Z. and X. M. and Y. L. Zhao Pengfei and Ye (Ed.), Advanced Graphic Communication, Printing and Packaging Technology (pp. 387–394). Springer Singapore, 2020.

[14] A. Ghadge, A. Duck, M. Er, N. Caldwell, Deceptive counterfeit risk in global supply chains, Supply Chain Forum: Int. J. 22 (2) (2021) 87–99, https://doi.org/10.1080/16258312.2021.1908844.

[15] Ö. Baruönü Latif, M. Kaytaz Yiğit, Ö. Kirezli, A review of counterfeiting research on demand side: Analyzing prior progress and identifying future directions, J. World Intellectual Property 21 (5–6) (2018) 458–480, https://doi.org/10.1111/jwip.12115.

[16] T. Staake, F. Thiesse, E. Fleisch, The emergence of counterfeit trade: a literature review, Eur. J. Mark. 43 (3/4) (2009) 320–349, https://doi.org/10.1108/03090560910935451.

[17] Y. Wang, J. Lin, T.-M. Choi, Gray market and counterfeiting in supply chains: A review of the operations literature and implications to luxury industries, Transport. Res. Part E: Logistics Transport. Rev. 133 (2020) 101823, https://doi.org/10.1016/j.tre.2019.101823.

[18] A. Tran, C.E. Boott, M.J. MacLachlan, Understanding the Self-Assembly of Cellulose Nanocrystals—Toward Chiral Photonic Materials, Adv. Mater. 32 (41) (2020), https://doi.org/10.1002/adma.201905876.

[19] Y. Ma, Y. Yu, P. She, J. Lu, S. Liu, W. Huang, Q. Zhao, On-demand regulation of photochromic behavior through various counterions for high-level security printing, Sci. Adv. 6 (16) (2020), https://doi.org/10.1126/sciadv.aaz2386.

[20] J. Park, J. Moon, H. Shin, D. Wang, M. Park, Direct-write fabrication of colloidal photonic crystal microarrays by ink-jet printing, J. Colloid Interface Sci. 298 (2) (2006) 713–719, https://doi.org/10.1016/j.jcis.2006.01.031.

[21] E.Y. Zlokazov, V.V. Kolyuchkin, D.S. Lushnikov, A.V. Smirnov, Computer-generated holograms application in security printing, Appl. Sci. 12 (7) (2022) 3289, https://doi.org/10.3390/app12073289.

[22] X. Bian, S. Haque, Counterfeit versus original patronage: Do emotional brand attachment, brand involvement, and past experience matter? J. Brand Manag. 27 (4) (2020) 438–451, https://doi.org/10.1057/s41262-020-00189-4.

[23] M. Orlowski, S. Lefebvre, L. Boman, The unintended effects of tamper-evident food closures, Int. J. Hosp. Manag. 107 (2022) 103315, https://doi.org/10.1016/j.ijhm.2022.103315.

[24] J. Zhang, R. Tan, Y. Liu, M. Albino, W. Zhang, M.M. Stevens, F.F. Loeffler, Printed smart devices for anti-counterfeiting allowing precise identification with household equipment, Nat. Commun. 15 (1) (2024) 1040, https://doi.org/10.1038/s41467-024-45428-3.

[25] Y. Agrawal, R. Shah, P. Prajapati, Anticounterfeit packaging technologies, J. Adv. Pharm. Technol. Res. 1 (4) (2010) 368, https://doi.org/10.4103/0110-5558.76434.

[26] M. Patel, R. Patel, C. Park, K. Cho, P. Kumar, C. Park, W.-G. Koh, Water-stable, biocompatible, and highly luminescent perovskite nanocrystals-embedded fiber-based paper for anti-counterfeiting applications, Nano Convergence 10 (1) (2023) 21, https://doi.org/10.1186/s40580-023-00366-6.

[27] K.L. Wlodarczyk, M. Ardron, N.J. Weston, D.P. Hand, Holographic watermarks and steganographic markings for combating the counterfeiting practices of high-value metal products, J. Mater. Process. Technol. 264 (2019) 328–335, https://doi.org/10.1016/j.jmatprotec.2018.09.020.

[28] Y. Liu, Y. Zheng, Y. Zhu, F. Ma, X. Zheng, K. Yang, X. Zheng, Z. Xu, S. Ju, Y. Zheng, T. Guo, L. Qian, F. Li, Unclonable perovskite fluorescent dots with fingerprint pattern for multilevel anticounterfeiting, ACS Appl. Mater. Interfaces 12 (35) (2020) 39649–39656, https://doi.org/10.1021/acsami.0c11103.

[29] J. Sang, J. Zhou, J. Zhang, H. Zhou, H. Li, Z. Ci, S. Peng, Z. Wang, Multilevel static-dynamic anticounterfeiting based on stimuli-responsive luminescence in a niobate structure, ACS Appl. Mater. Interfaces 11 (22) (2019) 20150–20156, https://doi.org/10.1021/acsami.9b03562.

[30] A. Smirnov, T. Pogosian, L. Zelenkov, S. Butonova, S. Makarov, A. Vinogradov, Structural color image augmented by inkjet printed perovskite patterning, Appl. Mater. Today 28 (2022) 101545, https://doi.org/10.1016/j.apmt.2022.101545.

[31] R. Ni, B. Qian, C. Liu, X. Liu, J. Qiu, 3D printing of resin composites doped with upconversion nanoparticles for anti-counterfeiting and temperature detection, Opt. Express 26 (19) (2018) 25481, https://doi.org/10.1364/OE.26.025481.

[32] Z. Quan, Q. Zhang, H. Li, S. Sun, Y. Xu, Fluorescent cellulose-based materials for information encryption and anti-counterfeiting, Coord. Chem. Rev. 493 (2023) 215287, https://doi.org/10.1016/j.ccr.2023.215287.

[33] X. Yu, H. Zhang, J. Yu, Luminescence anti-counterfeiting: From elementary to advanced, Aggregate 2 (1) (2021) 20–34, https://doi.org/10.1002/agt2.15.

[34] S.F. Iftekar, A. Aabid, A. Amir, M. Baig, Advancements and limitations in 3D printing materials and technologies: a critical review, Polymers 15 (11) (2023) 2519, https://doi.org/10.3390/polym15112519.

[35] A. Jandyal, I. Chaturvedi, I. Wazir, A. Raina, M.I. Ul Haq, 3D printing – A review of processes, materials and applications in industry 4.0, Sustain. Operat. Comput. 3 (2022) 33–42, https://doi.org/10.1016/j.susoc.2021.09.004.

[36] N. Shahrubudin, T.C. Lee, R. Ramlan, An overview on 3D printing technology: technological, materials, and applications, Procedia Manuf. 35 (2019) 1286–1296, https://doi.org/10.1016/j.promfg.2019.06.089.

[37] E. Caussin, C. Moussally, S. Le Goff, T. Fasham, M. Troizier-Cheyne, L. Tapie, E. Dursun, J.-P. Attal, P. François, Vat photopolymerization 3D printing in dentistry: a comprehensive review of actual popular technologies, Materials 17 (4) (2024) 950, https://doi.org/10.3390/ma17040950.

[38] R.J.N. Joshua, S.A. Raj, M.T. Hameed Sultan, A. Łukaszewicz, J. Józwik, Z. Oksiuta, K. Dziedzic, A. Tofil, F.S. Shahar, Powder bed fusion 3D printing in precision manufacturing for biomedical applications: a comprehensive review, Materials 17 (3) (2024) 769, https://doi.org/10.3390/ma17030769.

[39] Q. Luo, H. Liu, D. Li, J. Dai, L. Xia, J. Jiang, Y. Xu, B. Zeng, W. Luo, L. Dai, Carboxymethylcellulose hydrogels with stable carbon quantum dots: Enabling dynamic fluorescence modulation, automatic erasure, and secure information encryption, Carbohydr. Polym. 326 (2024) 121610, https://doi.org/10.1016/j.carbpol.2023.121610.

[40] H. Lv, S. Wang, Z. Wang, W. Meng, X. Han, J. Pu, Fluorescent cellulose-based hydrogel with carboxymethyl cellulose and carbon quantum dots for information storage and fluorescent anti-counterfeiting, Cellul. 29 (11) (2022) 6193–6204, https://doi.org/10.1007/s10570-022-04643-1.

[41] J. Wang, P. Du, Y.-I. Hsu, H. Uyama, Cellulose luminescent hydrogels loaded with stable carbon dots for duplicable information encryption and anti-counterfeiting, ACS Sustain. Chem. Eng. 11 (27) (2023) 10061–10073, https://doi.org/10.1021/acssuschemeng.3c01838.

[42] B.F. Bukit, F.A. Syamani, E. Rochima, C. Panatarani, W. Widiyastuti, D. Praseptiangga, N. Nazir, Y. Nurhamiyah, S. Agustina, Review of alginate-based composites for 3D printing material, Polym. Renewable Resour. (2024), https://doi.org/10.1177/20412479241227137.

[43] X. He, Q. Lu, A review of high internal phase Pickering emulsions: Stabilization, rheology, and 3D printing application, Adv. Colloid Interface Sci. 324 (2024) 103086, https://doi.org/10.1016/j.cis.2024.103086.

[44] J. Shen, S. Zhang, X. Fang, S. Salmon, Advances in 3D gel printing for enzyme immobilization, Gels 8 (8) (2022) 460, https://doi.org/10.3390/gels8080460.

[45] J. Zhao, N. He, A mini-review of embedded 3D printing: supporting media and strategies, J. Mater. Chem. B 8 (46) (2020) 10474–10486, https://doi.org/10.1039/D0TB01819H.

[46] W. Xu, S. Jambhulkar, Y. Zhu, D. Ravichandran, M. Kakarla, B. Vernon, D.G. Lott, J.L. Cornella, O. Shefi, G. Miquelard-Garnier, Y. Yang, K. Song, 3D printing for polymer/particle-based processing: A review, Compos. B Eng. 223 (2021) 109102, https://doi.org/10.1016/j.compositesb.2021.109102.

[47] L. Zhou, J. Fu, Y. He, A Review of 3D Printing Technologies for Soft Polymer Materials, Adv. Funct. Mater. 30 (28) (2020), https://doi.org/10.1002/adfm.202000187.

[48] X.N. Zhang, Q. Zheng, Z.L. Wu, Recent advances in 3D printing of tough hydrogels: A review, Compos. B Eng. 238 (2022) 109895, https://doi.org/10.1016/j.compositesb.2022.109895.

[49] H. Herrada-Manchón, M.A. Fernández, E. Aguilar, Essential guide to hydrogel rheology in extrusion 3D printing: how to measure it and why it matters? Gels 9 (7) (2023) 517, https://doi.org/10.3390/gels9070517.

[50] C. Dannert, B.T. Stokke, R.S. Dias, Nanoparticle-Hydrogel Composites: From Molecular Interactions to Macroscopic Behavior, Polymers 11 (2) (2019) 275, https://doi.org/10.3390/polym11020275.

[51] W. Gao, Y. Zhang, Q. Zhang, L. Zhang, Nanoparticle-Hydrogel: A Hybrid Biomaterial System for Localized Drug Delivery, Ann. Biomed. Eng. 44 (6) (2016) 2049–2061, https://doi.org/10.1007/s10439-016-1583-9.

[52] J. Zaragoza, S. Fukuoka, M. Kraus, J. Thomin, P. Asuri, Exploring the Role of Nanoparticles in Enhancing Mechanical Properties of Hydrogel Nanocomposites, Nanomaterials 8 (11) (2018) 882, https://doi.org/10.3390/nano8110882.
[53] Z. Sun, Z. Li, K. Qu, Z. Zhang, Y. Niu, W. Xu, C. Ren, A review on recent advances in gel adhesion and their potential applications, J. Mol. Liq. 325 (2021) 115254, https://doi.org/10.1016/j.molliq.2020.115254.
[54] D. Trache, M.H. Hussin, M.K.M. Haafiz, V.K. Thakur, Recent progress in cellulose nanocrystals: sources and production, Nanoscale 9 (5) (2017) 1763–1786, https://doi.org/10.1039/C6NR09494E.
[55] S. Xie, X. Zhang, M.P. Walcott, H. Lin, Applications of cellulose nanocrystals: a review, Eng. Sci. (2018), https://doi.org/10.30919/es.1803302.
[56] V. Cherpak, V.F. Korolovych, R. Geryak, T. Turiv, D. Nepal, J. Kelly, T.J. Bunning, O.D. Lavrentovich, W.T. Heller, V.V. Tsukruk, Robust Chiral Organization of Cellulose Nanocrystals in Capillary Confinement, Nano Lett. 18 (11) (2018) 6770–6777, https://doi.org/10.1021/acs.nanolett.8b02522.
[57] V.F. Korolovych, V. Cherpak, D. Nepal, A. Ng, N.R. Shaikh, A. Grant, R. Xiong, T. J. Bunning, V.V. Tsukruk, Cellulose nanocrystals with different morphologies and chiral properties, Polymer 145 (2018) 334–347, https://doi.org/10.1016/j.polymer.2018.04.064.
[58] Anuj Kumar, Stefan Ioan Voicu, Vijay Kumar Thakur, 3D printable Gel-inks for Tissue Engineering (A. Kumar, S. I. Voicu, & V. K. Thakur, Eds.). Springer Singapore, 2021. 10.1007/978-981-16-4667-6.
[59] M. Tuerhong, Y. Xu, X.-B. Yin, Review on carbon dots and their applications, Chin. J. Anal. Chem. 45 (1) (2017) 139–150, https://doi.org/10.1016/S1872-2040(16)60990-8.
[60] C. Xia, S. Zhu, T. Feng, M. Yang, B. Yang, Evolution and Synthesis of Carbon Dots: From Carbon Dots to Carbonized Polymer Dots. Advanced, Science 6 (23) (2019), https://doi.org/10.1002/advs.201901316.
[61] Z. Kang, S.-T. Lee, Carbon dots: advances in nanocarbon applications, Nanoscale 11 (41) (2019) 19214–19224, https://doi.org/10.1039/C9NR05647E.
[62] J. Zhu, X. Bai, J. Bai, G. Pan, Y. Zhu, Y. Zhai, H. Shao, X. Chen, B. Dong, H. Zhang, H. Song, Emitting color tunable carbon dots by adjusting solvent towards light-emitting devices, Nanotechnology 29 (8) (2018) 085705, https://doi.org/10.1088/1361-6528/aaa321.
[63] A.M. Brouwer, Standards for photoluminescence quantum yield measurements in solution (IUPAC Technical Report), Pure Appl. Chem. 83 (12) (2011) 2213–2228, https://doi.org/10.1351/PAC-REP-10-09-31.
[64] Z. Qian, J. Ma, X. Shan, H. Feng, L. Shao, Highly Luminescent N-Doped Carbon Quantum Dots as an Effective Multifunctional Fluorescence Sensing Platform. 2254–2263, 2014. 10.1002/chem.201304374.
[65] Z. Qian, J. Ma, X. Shan, H. Feng, L. Shao, J. Chen, Highly luminescent N-Doped carbon quantum dots as an effective multifunctional fluorescence sensing platform, Chem. – A Eur. J. 20 (8) (2014) 2254–2263, https://doi.org/10.1002/chem.201304374.
[66] B.T. Hoan, P.D. Tam, V.H. Pham, Green synthesis of highly luminescent carbon quantum dots from lemon juice, J. Nanotechnol. 2019 (2019), https://doi.org/10.1155/2019/2852816.
[67] S.S. Monte-Filho, S.I.E. Andrade, M.B. Lima, M.C.U. Araujo, Synthesis of highly fluorescent carbon dots from lemon and onion juices for determination of riboflavin in multivitamin/mineral supplements, J. Pharm. Anal. 9 (3) (2019) 209–216, https://doi.org/10.1016/j.jpha.2019.02.003.
[68] M.Y. Pudza, Z.Z. Abidin, S.A. Rashid, F.M. Yasin, A.S.M. Noor, M.A. Issa, Eco-friendly sustainable fluorescent carbon dots for the adsorption of heavy metal ions in aqueous environment, Nanomaterials 10 (2) (2020), https://doi.org/10.3390/nano10020315.
[69] M. Xu, G. He, Z. Li, F. He, F. Gao, Y. Su, L. Zhang, Z. Yang, Y. Zhang, A green heterogeneous synthesis of N-doped carbon dots and their photoluminescence applications in solid and aqueous states, Nanoscale 6 (17) (2014) 10307–10315, https://doi.org/10.1039/C4NR02792B.
[70] S. Peng, S. Sun, Y. Zhu, J. Qiu, H. Yang, Colourful 3D anti-counterfeiting label using nanoscale additive manufacturing, Virtual Phys. Prototyping 18 (1) (2023), https://doi.org/10.1080/17452759.2023.2179929.
[71] F. Ashrafi Tafreshi, Z. Fatahi, S.F. Ghasemi, A. Taherian, N. Esfandiari, Ultrasensitive fluorescent detection of pesticides in real sample by using green carbon dots, PLoS One 15 (3) (2020) e0230646.
[72] N. Atykyan, V. Revin, V. Shutova, Raman and FT-IR Spectroscopy investigation the cellulose structural differences from bacteria Gluconacetobacter sucrofermentans during the different regimes of cultivation on a molasses media, AMB Express 10 (1) (2020) 84, https://doi.org/10.1186/s13568-020-01020-8.
[73] A. Verhagen, A. Kelarakis, Carbon dots for forensic applications: a critical review, Nanomaterials 10 (8) (2020) 1535, https://doi.org/10.3390/nano10081535.
[74] K. Guo, P. Wei, Y. Xie, X. Huang, Smart ultra-stable foams stabilized using cellulose nanocrystal (CNC) gels via noncovalent bonding, Chem. Commun. 58 (30) (2022) 4723–4726, https://doi.org/10.1039/D2CC00289B.
[75] P. Martin, G. Vasilyev, G. Chu, M. Boas, A. Arinstein, E. Zussman, pH-Controlled network formation in a mixture of oppositely charged cellulose nanocrystals and poly(allylamine), J. Polym. Sci. B: Polymer Physics 57 (22) (2019) 1527–1536, https://doi.org/10.1002/polb.24898.
[76] S.M. Morozova, T.G. Statsenko, E.O. Ryabchenko, A. Gevorkian, V. Adibnia, M. S. Lozhkin, A.V. Kireynov, E. Kumacheva, Multicolored Nanocolloidal Hydrogel Inks, Adv. Funct. Mater. 31 (52) (2021), https://doi.org/10.1002/adfm.202105470.
[77] Y. Sun, X. Wang, C. Wang, D. Tong, Q. Wu, K. Jiang, Y. Jiang, C. Wang, M. Yang, Red emitting and highly stable carbon dots with dual response to pH values and ferric ions, Microchim. Acta 185 (1) (2018) 83, https://doi.org/10.1007/s00604-017-2544-1.
[78] Z. Jiang, L. Tang, X. Gao, W. Zhang, J. Ma, L. Zhang, Solvent regulation approach for preparing cellulose-nanocrystal-reinforced regenerated cellulose fibers and their properties, ACS Omega 4 (1) (2019) 2001–2008, https://doi.org/10.1021/acsomega.8b03601.
[79] S. Wang, Y. Yang, A. Lu, L. Zhang, Construction of cellulose/ZnO composite microspheres in NaOH/zinc nitrate aqueous solution via one-step method, Cellul. 26 (1) (2019) 557–568, https://doi.org/10.1007/s10570-018-2201-9.
[80] X. Wu, Z. Wang, G. Shao, B. Qin, Y. Wang, T. Wang, Z. Liu, Y. Fu, Supramolecular cellulose-based heavy metal adsorbent for efficient and accurate removal of cobalt (II) for water treatment, React. Funct. Polym. 194 (2024) 105759, https://doi.org/10.1016/j.reactfunctpolym.2023.105759.
[81] N. Abidi, FTIR Microspectroscopy, Springer International Publishing (2021), https://doi.org/10.1007/978-3-030-84426-4.
[82] Z. Dai, J. Deng, L. Ansaloni, S. Janakiram, L. Deng, Thin-film-composite hollow fiber membranes containing amino acid salts as mobile carriers for CO2 separation, J. Membr. Sci. 578 (2019) 61–68, https://doi.org/10.1016/j.memsci.2019.02.023.
[83] L. Rinawati, R.E. Nugraha, R. Mahdia, I. Munifa, U. Chasanah, S. Wahyuningsih, A. Ramelan, Increasing the effectiveness of pesticides based urea nanofertilizer encapsulated nanosilica with addition of rice husk TiO 2 additive substances, J. Chem. Pharm. Res. 2015 (2015) 85–89.
[84] Z. Ren, H. Huang, J. Zhang, H. Qi, M. Xu, X. Wang, Cellulose hydrogel is a novel carbon-source and doping-material-carrier to prepare fluorescent carbon dots for intracellular bioimaging, SN Appl. Sci. 2 (1) (2020) 17, https://doi.org/10.1007/s42452-019-1794-4.
[85] L. Zhang, Q. Zhang, J. Yu, J. Ma, Z. Wang, Y. Fan, S. Kuga, Strengthened cellulosic gels by the chemical gelation of cellulose via crosslinking with TEOS, Cellul. 26 (18) (2019) 9819–9829, https://doi.org/10.1007/s10570-019-02765-7.
[86] L. Cui, X. Ren, M. Sun, H. Liu, L. Xia, Carbon dots: synthesis, Properties Appl. Nanomater. 11 (12) (2021) 3419, https://doi.org/10.3390/nano11123419.
[87] H. Ehtesabi, Z. Hallaji, S. Najafi Nobar, Z. Bagheri, Carbon dots with pH-responsive fluorescence: a review on synthesis and cell biological applications, Microchim. Acta 187 (2) (2020) 150, https://doi.org/10.1007/s00604-019-4091-4.
[88] F.C. Godoi, S. Prakash, B.R. Bhandari, 3d printing technologies applied for food design: Status and prospects, J. Food Eng. 179 (2016) 44–54, https://doi.org/10.1016/j.jfoodeng.2016.01.025.
[89] S. Russo Spena, N. Grizzuti, D. Tammaro, Linking Processing Parameters and Rheology to Optimize Additive Manufacturing of k-Carrageenan Gel Systems, Gels 8 (8) (2022) 493, https://doi.org/10.3390/gels8080493.
[90] B.K. Barman, Ø. Sele Handegård, A. Hashimoto, T. Nagao, Carbon dot/cellulose-based transparent films for efficient UV and high-energy blue light screening, ACS Sustain. Chem. Eng. 9 (29) (2021) 9879–9890, https://doi.org/10.1021/acssuschemeng.1c02791.
[91] J. Liao, K.A. Pham, V. Breedveld, Rheological characterization and modeling of cellulose nanocrystal and TEMPO-oxidized cellulose nanofibril suspensions, Cellul. 27 (7) (2020) 3741–3757, https://doi.org/10.1007/s10570-020-03048-2.
[92] X. Wang, X. Teng, X. Sun, W. Pan, J. Wang, Carbon dots with aggregation induced quenching effect and solvatochromism for the detection of H2O in organic solvents, Spectrochim. Acta A Mol. Biomol. Spectrosc. 267 (2022) 120547, https://doi.org/10.1016/j.saa.2021.120547.
[93] F. Zu, F. Yan, Z. Bai, J. Xu, Y. Wang, Y. Huang, X. Zhou, The quenching of the fluorescence of carbon dots: A review on mechanisms and applications, Microchim. Acta 184 (7) (2017) 1899–1914, https://doi.org/10.1007/s00604-017-2318-9.
[94] A.E. Patterson, C. Chadha, I.M. Jasiuk, J.T. Allison, Tensile behavior of individual fibers and films made via material extrusion additive manufacturing, Next Materials 1 (1) (2023) 100002, https://doi.org/10.1016/j.nxmate.2023.100002.